Updated Zeeman effect splitting coefficients for molecular oxygen in planetary applications

Richard Larsson [a,*], Boy Lankhaar [b], Patrick Eriksson [c]

[a] *Max-Planck-Institut für Sonnensystemforschung, Justus-von-Liebig-Weg 3, Göttingen, 37077, Germany*
[b] *Department of Space, Earth and Environment, Chalmers University of Technology, Onsala Space Observatory, Onsala, 439 92, Sweden*
[c] *Department of Earth and Space Sciences, Chalmers University of Technology, Gothenburg, SE-41296, Sweden*

A R T I C L E   I N F O

A B S T R A C T

We comment on a common practice to use pure Hund case (b) Zeeman parameters in planetary atmospheric radiative transfer applications involving molecular oxygen. A detailed theoretical formulation is presented for the Zeeman splitting coefficients of molecular oxygen in its ground vibronic state, taking also the relevant fine-structure interactions into account. The updated Zeeman parameters are compared to the simplified Hund case (b) approach used in earlier works. The biggest differences between the output of these formulations occur for states with low rotational energy, and the differences are greater for $^{16}O^{18}O$ than for $^{16}O_2$. To get the order of magnitude error introduced by the simplification of the splitting coefficient computations, we perform a limited case study of forward simulations for a few space-borne and ground-based instruments. Our analysis shows that using simplified Zeeman coefficients introduces errors in the forward modelled radiation varying from insignificant up to 10 K.

1. Introduction

The main reason to observe microwave emissions of molecular oxygen in earth's atmosphere is to retrieve a vertical temperature profile. A secondary reason for such observations is more recent: To retrieve the magnetic field from the Zeeman split and polarized line profile. In either case, accurate forward model calculations are required, and since molecular oxygen transitions are affected by the magnetic field, such a forward model must take the Zeeman [1] effect into account. Several instruments observe the Zeeman effect on molecular oxygen transitions in earth's atmosphere, either by resolving the fine features of the line shape, or sampling the line absorption as a whole. Instruments that have been — or are — measuring the Zeeman effect from space or ground in earth's atmosphere include the Odin Sub-Millimetre Radiometer (Odin/SMR; [2]), the Earth Observation Systems Aura Microwave Limb Sounder (EOS Aura/MLS; [3]), the Special Sensor Microwave Imager/Sounder (SSMIS; [4,5]), the Millimeter-wave Atmospheric Sounder (MAS; [6]), the Temperature Radiometer (TEMPERA; [7]), and the 2.5 m millimetre-wave telescope (POM-2; [8]). Others have proposed to use the Zeeman effect to retrieve either variations in earth's magnetic field [9], or on other planets [10,11]. The standard approach to

model molecular oxygen's Zeeman effect in planetary atmospheric applications, ever since Lenoir [12,13] first published on the matter, has been to assume that it acts as a simplified Hund case (b) molecule. This approach has been used by Liebe [14], Rosenkranz and Staelin [15], Pardo et al. [8], Schwartz et al. [3], and Larsson et al. [16]. Especially for transitions between levels with low rotational energy (low J_N), this approximation becomes problematic as the perfect Hund's case (b) description of molecular oxygen breaks down with decreasing J_N. In this paper, instead of describing molecular oxygen as a perfect Hund's case (b) molecule, we adopt the latest model on its rotational fine-structure states Drouin et al. [17] as the basis for the calculation of molecular oxygen's Zeeman effect, while using experimental data for all relevant Zeeman interactions [18,19]. We will use our updated model on molecular oxygen's Zeeman effect in representative case studies to asses its impact on relevant remote sensing experiments.

The structure of this paper is as follows. The next section shows the detailed computations for the Zeeman effect and derives from them the simplified approach. The section that follows describe the method used to perform the computations that yielded the results of the fourth section. Lastly, we present our conclusions.

2. Theory

Molecular oxygen is an open-shell diatomic molecule with two unpaired electrons. The microwave spectral lines of atmospheric

* Corresponding author.
E-mail address: larsson@mps.mpg.de (R. Larsson).

molecular oxygen usually occur in the ground-electronic state, which is a $^3\Sigma$ state; having a total electron-spin $S = 1$ and zero orbital angular momentum projection $\Lambda = 0$. Spectral fine-structure is introduced via mutual interactions between the electrons, the spin-spin interaction, the interaction of the electron-spins with the molecular rotation, and the rotational motion of the molecule itself. We note the effective fine-structure Hamiltonian of O_2 as [20]

$$\hat{H}_{\text{eff}} = \hat{H}_{\text{ss}} + \hat{H}_{\text{sr}} + \hat{H}_{\text{rot}}. \tag{1}$$

We call this Hamiltonian an effective one, because in the respective terms for the individual interactions, the couplings between different vibronic states that give rise to these interactions, have been conveniently reduced to an effective coupling constant, and an associated coupling of the appropriate angular momentum operators [17,20]:

$$
\begin{aligned}
\hat{H}_{\text{ss}} &= \left(\lambda + \lambda_D \widehat{\boldsymbol{N}}^2 + \lambda_H \widehat{\boldsymbol{N}}^4\right)\frac{2}{3}\left(3\hat{S}_z^2 - \widehat{\boldsymbol{S}}^2\right) \\
\mathcal{H}_{\text{sr}} &= \left(\gamma + \gamma_D \widehat{\boldsymbol{N}}^2 + \gamma_H \widehat{\boldsymbol{N}}^4\right)\widehat{\boldsymbol{N}} \cdot \widehat{\boldsymbol{S}}, \\
\mathcal{H}_{\text{rot}} &= B\widehat{\boldsymbol{N}}^2 - D\widehat{\boldsymbol{N}}^4 + H\widehat{\boldsymbol{N}}^6,
\end{aligned}
\tag{2}
$$

where λ and γ are the spin-spin and the spin-rotation constants (subscript D and H refer to the 1st and 2nd order centrifugal distortion constants), and B, D, and H are the rotational, rotational centrifugal distortion constants of 1st order, and rotational centrifugal distortion constants of 2nd order, respectively. The angular momentum operators for the rotation and spin are $\widehat{N}$ and $\widehat{S}$, and the projection operator, $\hat{S}_z$, is associated with the intermolecular axis. One obtains matrix elements for the fine-structure in a particular angular momentum basis. The individual angular momenta can be coupled in different ways. The different coupling schemes are known as the Hund's cases. Molecular oxygen is very well described as a Hund's case (b) molecule, having basis functions [20]

$$\{|\eta, [(N, \Lambda)N, S]JM_J\rangle\}, \tag{3}$$
$$N = 0, 1, \cdots$$
$$J \in |N - S|, |N - S| + 1, \cdots, N + S$$
$$M_J \in -J, -J + 1, \cdots, J$$

where we have used $\Lambda = 0$, and η is the collection of all other quantum numbers. Matrix elements of Eq. (2) in the basis of Eq. (3) can be readily obtained via angular momentum algebra [20]. From these matrix-elements, one observes that the spin-spin interaction couples $N = N \pm 2$ states, so the perfect Hund's case (b) description breaks down.

When an external magnetic field is introduced, the magnetic sub-levels will split up according to the Zeeman effect. The Zeeman effect of molecular oxygen comes from the electron spin, $\hat{H}_{\text{bs}} + \hat{H}_{\text{bas}}$, where the latter term describes the anisotropic part of the spin Zeeman interactions, and the molecular rotation, $\hat{H}_{\text{br}}$. Rotational and anisotropic spin Zeeman effects are higher-order Zeeman effects, and are about three orders of magnitude smaller than the spin Zeeman effect. We denote [as 19, did]

$$
\begin{aligned}
\hat{H}_{\text{Zeeman}} &= \hat{H}_{\text{bs}} + \hat{H}_{\text{bas}} + \hat{H}_{\text{br}} \\
&= \mu_B \|\vec{B}\| \left(g_S \hat{S}_z + g_l^e \sum_{q=\pm} D_{0q}^{(1)*}(\alpha\beta\gamma)\hat{S}_q - g_r \hat{N}_z\right),
\end{aligned}
\tag{4}
$$

as the Zeeman Hamiltonian, where g_S, g_l^e, and g_r are the spin, anisotropic spin, and rotational g-factors, the magnetic field is given by $\|\vec{B}\|$, μ_B is the Bohr-magneton and $D_{0q}^{(1)*}(\alpha\beta\gamma)$ is a Wigner-D matrix element of the Euler angles, and $\hat{S}_q$ are elements of the spin-operator in a spherical basis. The Zeeman Hamiltonians matrix elements in the case (b) basis are again readily obtained via angular momentum algebra [20]. They yield coupling elements between $N = N \pm 1$ states and $J = J \pm 1$ states, but we will

Table 1

Molecular constants and g-factors for $^{16}O_2$ and $^{16}O^{18}O$. The g-factors of the Zeeman interactions fitted by Bowers et al. and Christensen and Veseth [18,19] and the molecular constants come from Drouin et al. [17].

	$^{16}O_2$	$^{16}O^{18}O$
g_S	2.002084	2.002025
g_l^e	2.77×10^{-3}	2.813×10^{-3}
g_r	-1.16×10^{-4}	-1.26×10^{-4}
B (MHz)	43100.44276	40707.38657
D (kHz)	145.1271	129.4142
H (mHz)	49	
λ (MHz)	59501.3438	59499.0375
λ_D (kHz)	58.3680	54.9777
λ_H (mHz)	290.8	272.1
γ (MHz)	-252.58634	-238.51530
γ_D (Hz)	-243.42	-217.77
γ_H (mHz)	-1.46	-1.305

not be concerned with these, because at the magnetic fields we are interested in, a perturbative treatment of the Zeeman effects is warranted. Previous investigation to effects of magnetic fields on atmospheric spectra made use of a simplified model of the fine-structure states of molecular oxygen. By assuming a perfect Hund's case (b) description, effectively, the off-diagonal elements of the fine-structure Hamiltonian are neglected, and the eigenstates are the pure basis-functions as in Eq. (3). Also, the higher order effects from the rotational and anisotropic spin Zeeman interactions are neglected in the simplified approach. This yields the following simplified expressions for the Landé g-factor for a certain level J_N e.g., [16]

$$g_{J_N} = g_S \frac{J(J+1) + S(S+1) - N(N+1)}{2J(J+1)}. \tag{5}$$

Although this is a good approximation, a better model is readily obtained by considering the higher-order Zeeman interactions, and by also considering the off-diagonal elements of $\hat{H}_{\text{eff}}$, that effectively mix the individual fine-structure states. It was also in this way that Christensen and Veseth [19] and Bowers et al. [18] determined the Zeeman parameters of molecular oxygen, as reproduced in Table 1, by fitting Eqs. (2) and (4) to their experiments.

For convenience and shortness, henceforth in this paper "new" refers to the detailed theory or g_{J_N}-coefficients derived from Eq. (4), and "old" refers to the simplified theory or g_{J_N}-coefficients derived from Eq. (5). While the theory itself is not new, our application of it is.

3. Method

3.1. Fine-structure and Zeeman effects

In order to compute molecular oxygen's Zeeman effects, we first have to model its fine-structure in the absence of a magnetic field. Because of the off-diagonal elements in the spin-spin interactions, a pure Hund's case (b) description of the eigenstates is not warranted. We recognize Λ, S, J and M_J as good quantum numbers, as well as the collection η of vibronic quantum numbers. The elements of the spin-spin Hamiltonian in the Hund's case (b) are nonzero also when $N' = N \pm 2$. Because N takes values $J - 1$, J, $J + 1$, we have for the levels with total angular momentum J, the follow-

ing representative Hamiltonians

$$
\begin{aligned}
H_{\eta\Lambda SJ}^{N=J} &= \langle \eta, [(N=J,\Lambda)N=J,S]JM_J|\hat{H}_{\text{eff}}|\eta, [(N=J,\Lambda)N=J,S]JM_J\rangle \\
&= BJ(J+1) - DJ^2(J+1)^2 + HJ^3(J+1)^3 \\
&\quad - \left[\gamma + \gamma_D J(J+1) + \gamma_H J^2(J+1)^2\right] \\
&\quad + \tfrac{2}{3}\left[\lambda + \lambda_D J(J+1) + \lambda_H J^2(J+1)^2\right],
\end{aligned}
\tag{6}
$$

$$
\boldsymbol{H}_{\eta\Lambda SJ}^{N\neq J} = \begin{pmatrix} H_{\eta\Lambda SJ}^{J-1,J-1} & H_{\eta\Lambda SJ}^{J-1,J+1} \\ H_{\eta\Lambda SJ}^{J+1,J-1} & H_{\eta\Lambda SJ}^{J+1,J+1} \end{pmatrix},
$$

where we have decomposed the initial 3×3 Hamiltonian in two parts, because of absence of coupling-elements between them. Indeed, it is the $J_{N=J}$ states that can be described with a pure Hund's case (b) basis function

$$
|J_{N=J}M_J\rangle = |\eta, [(N=J,\Lambda)N=J,S]JM_J\rangle
\tag{7}
$$

and lend themselves to the approximation of the 'old' method (provided the additional higher-order Zeeman interactions we described earlier are accounted for). The individual elements of $\boldsymbol{H}_{\eta\Lambda SJ}^{N\neq J}$ are

$$
\begin{aligned}
H_{\eta\Lambda SJ}^{J-1,J-1} &= \langle \eta, [(N=J-1,\Lambda)N=J-1,S]\,JM_J|\hat{H}_{\text{eff}}|\eta, \\
&\quad [(N=J-1,\Lambda)N=J-1,S]\,JM_J\rangle \\
&= BJ(J-1) - DJ^2(J-1)^2 + HJ^3(J-1)^3 \\
&\quad + \left[\gamma + \gamma_D J(J-1) + \gamma_H J^2(J-1)^2\right](J-1) \\
&\quad + \left[\lambda + \lambda_D J(J-1) + \lambda_H J^2(J-1)^2\right]\left(\tfrac{2}{3} - \tfrac{2J}{2J+1}\right)
\end{aligned}
$$

$$
\begin{aligned}
H_{\eta\Lambda SJ}^{J+1,J+1} &= \langle \eta, [(N=J+1,\Lambda)N=J+1,S]\,JM_J|\hat{H}_{\text{eff}}|\eta, \\
&\quad [(N=J+1,\Lambda)N=J+1,S]\,JM_J\rangle \\
&= B(J+2)(J+1) - D(J+2)^2(J+1)^2 + H(J+2)^3(J+1)^3 \\
&\quad - \left[\gamma + \gamma_D(J+2)(J+1) + \gamma_H(J+2)^2(J+1)^2\right](J+2) \\
&\quad + \left[\lambda + \lambda_D(J+2)(J+1) + \lambda_H(J+2)^2(J+1)^2\right] \\
&\quad \times \left(\tfrac{2}{3} - \tfrac{2(J+1)}{2J+1}\right)
\end{aligned}
$$

$$
\begin{aligned}
H_{\eta\Lambda SJ}^{J-1,J+1} &= \langle \eta, [(N=J-1,\Lambda)N=J-1,S]\,JM_J|\hat{H}_{\text{eff}}|\eta, \\
&\quad [(N=J+1,\Lambda)N=J+1,S]\,JM_J\rangle \\
&= H_{\eta\Lambda SJ}^{J+1,J-1} = \left[\lambda + \lambda_D(J^2+J+1) + \lambda_H(J^2+J+1)^2\right]\frac{2\sqrt{J(J+1)}}{2J+1},
\end{aligned}
\tag{8}
$$

where we have used that $S=1$ for ground-state molecular oxygen. This symmetric 2×2 Hamiltonian can be diagonalized analytically yielding the following eigenfunctions for the $J_{N\neq J}$ states

$$
\begin{aligned}
|J_{N=J-1}M_J\rangle &= \cos\left(\phi_{\eta\Lambda SJ}\right)|\eta, [(N=J-1,\Lambda)N=J-1,S]JM_J\rangle \\
&\quad + \sin\left(\phi_{\eta\Lambda SJ}\right)|\eta, [(N=J+1,\Lambda)N=J+1,S]JM_J\rangle, \\
|J_{N=J+1}M_J\rangle &= \cos\left(\phi_{\eta\Lambda SJ}\right)|\eta, [(N=J+1,\Lambda)N=J+1,S]JM_J\rangle \\
&\quad - \sin\left(\phi_{\eta\Lambda SJ}\right)|\eta, [(N=J-1,\Lambda)N=J-1,S]JM_J\rangle,
\end{aligned}
\tag{9}
$$

where the diagonalization angle $\phi_{\eta\Lambda SJ}$ is obtained from the ratio of off- and diagonal elements

$$
\tan\left(2\phi_{\eta\Lambda SJ}\right) = \frac{2H_{\eta\Lambda SJ}^{J+1,J-1}}{H_{\eta\Lambda SJ}^{J-1,J-1} - H_{\eta\Lambda SJ}^{J+1,J+1}}.
\tag{10}
$$

Eqs. (7) and (9) describe the fine-structure eigenstates that we will use in modeling the Zeeman-effect of a certain fine-structure level.

Because of the weak magnetic fields we are considering, it is warranted to use a perturbative approach in computing the Zeeman effects. In such a perturbative approach, Zeeman-effects are proportional to the magnetic field and some proportionality-constant, called the g-factor. We define the g-factor for a particular state J_N from the relation

$$
\langle J_N M_J|\hat{H}_{\text{Zeeman}}|J_N M_J\rangle = \mu_B g_{J_N}||\vec{B}||M_J,
$$

or,

$$
g_{J_N} = \frac{\langle J_N M_J = 1|\hat{H}_{\text{Zeeman}}|J_N M_J = 1\rangle}{\mu_B||\vec{B}||}.
\tag{11}
$$

We can evaluate $\langle J_N M_J = 1|\hat{H}_{\text{Zeeman}}|J_N M_J = 1\rangle$ using Eqs. (4), (7) and (9), which yields

$$
\begin{aligned}
g_{J_{N=J-}} &= (g_S + g_r)\left[\frac{\cos^2\left(\phi_{\eta\Lambda SJ}\right)}{J} - \frac{\sin^2\left(\phi_{\eta\Lambda SJ}\right)}{J+1}\right] \\
&\quad + \frac{2g_l^e \cos\left(2\phi_{\eta\Lambda SJ}\right)}{2J+1} - g_r, \\
g_{J_{N=J}} &= \frac{g_S + g_r}{J(J+1)} - g_r, \\
g_{J_{N=J+1}} &= (g_S + g_r)\left[\frac{\sin^2\left(\phi_{\eta\Lambda SJ}\right)}{J} - \frac{\cos^2\left(\phi_{\eta\Lambda SJ}\right)}{J+1}\right] \\
&\quad - \frac{2g_l^e \cos\left(2\phi_{\eta\Lambda SJ}\right)}{2J+1} - g_r.
\end{aligned}
\tag{12}
$$

The level specific g-factors from Eq. (12) are evaluated by computing the $\phi_{\eta\Lambda SJ}$ from the matrix-elements of Eq. (9) using the molecular constants reported in [17] and inserting them in Eq. (10). Table 1 reports the experimentally determined g-factors we use for g_S, g_l^e and g_r. The level-specific g-factors will be used to compute the magnetic field-dependent splitting of the magnetic sub-levels. This splitting will subsequently lead to a splitting in the spectrum of a transition associated with that level. In the following subsection, we will outline how this spectral splitting will affect the propagation of (polarized) radiation.

3.2. Absorption profile computations

The method for all spectral absorption profile computations follows Larsson et al. [16]. As a brief update to that paper, the software has been changed so that the relative strength of a Zeeman split line is computed by

$$
S_Z = C\begin{pmatrix} J'' & 1 & J' \\ M_J'' & M_J' - M_J'' & -M_J' \end{pmatrix}\begin{pmatrix} J'' & 1 & J' \\ M_J'' & M_J' - M_J'' & -M_J' \end{pmatrix},
\tag{13}
$$

where $C = 1.5$ for $M_J' - M_J'' = 0$ and $C = 0.75$ otherwise, and where $(:\,:\,:)$ are Wigner 3j-symbols. In [16] this expression was a table with conditions for J, ΔJ, M_J, and ΔM_J, but since the shorter expression gives the same results, and is fast to execute with the Wigner algorithm by Johansson and Forssén [21], we changed the internal code to be more maintainable. As a brief review of the spectral absorption profile computations, the central frequency of a certain line, $J_N'' - J_N'$, is displaced or Zeeman-shifted to appear as several lines, one for each valid $M_J'' - M_J'$ transition, following

$$
\Delta f_Z = \frac{\mu_B}{h}\left(g_{J_N''}M_J'' - g_{J_N'}M_J'\right)||\vec{B}||,
\tag{14}
$$

and the line shape of the displaced line is given by

$$
F_Z = \frac{1}{\Gamma_D\sqrt{\pi}}w(z), \quad z = \frac{f - f_0 - \Delta f_Z + i\Gamma_P}{\Gamma_D},
\tag{15}
$$

so that the polarized absorption is the sum over all displaced components

$$
\mathbf{K} = n S_{J_N'' J_N'} \sum_Z S_Z F_Z \mathbf{\Phi}_Z.
\tag{16}
$$

Here single prime gives the upper state, double prime gives the lower state, $||\vec{B}||$ is the magnetic field strength, f is the frequency, f_0 is the un-split line frequency, Γ_P is the pressure broadening half-width at half maximum, Γ_D is the Doppler broadening half-width at half maximum divided by $\sqrt{\ln 2}$, $w(z)$ is the Faddeeva function, n is the number density of the molecule in question, $S_{J''_N J'_N}$ is the strength of the un-split line, and Φ_Z is the Mueller matrix describing how the radiation is polarized by the propagation [see 16, for these matrices, and a more thorough description of the radiative transfer calculations being performed]. We neglect pressure induced frequency shifts in these expressions because they are not important for the molecular oxygen transitions of interest here. We also neglect line mixing in this expression but note that we consider it in the forward simulations [22] below. The code is implemented in the Atmospheric Radiative Transfer Simulator ARTS; [23, 24], which can be found via http://radiativetransfer.org/, and is available for all to use under a copy-left license.

4. Results and discussions

Principally, the improvement of the Zeeman-coefficients comes from the improved quality of the description of the fine-structure in our new model. The fine-structure model we use comes from [17] and fits the 9 parameters reported in Eq. (6) to an experimental data-set of 51 lines for $^{16}O_2$ and 83 lines for $^{16}O^{18}O$. The fitting-parameters include 1st and 2nd order distortion effects that are required for an accurate description of high-J_N transitions, but experiments have only been carried out up to transitions including $J_N = 40_{39}$ levels. It is not clear how well these parameters would describe the higher J_N-fine structure states, that we also include in our data-set here. However, we recognize in Eq. (9), that the off-diagonal elements in the fine-structure Hamiltonian abate with respect to the diagonal elements, so that a pure Hund's case (b) description becomes increasingly justified, and fine-structure effects on the Zeeman-parameters gradually disappear. This is also reflected and well-described in the model we employ. The second, somewhat less pronounced, improvement to the Zeeman-coefficients comes from including the higher-order rotational- and anisotropic spin-Zeeman effects. From Eq. (12), and taking into account that g_l^e and g_r are both $\sim 10^{-3} g_S$, we see that especially for low J_N, the impact of these improvements is significant but small. For higher J_N, including also rotational Zeeman effects become increasingly important to accurately model molecular oxygen's Zeeman effects.

Table 2 contains the computed Zeeman coefficients for the energy levels $J \leq 50$ in ground-vibrational state of both $^{16}O_2$ and $^{16}O^{18}O$. Fig. 1 shows the same numbers graphically and compares them to the old approach of Eq. (5). From the figure and table, the $J_{N=J}$ energy states have similar g_{J_N}-coefficients using the new formulation and the old formulation for all $J_{N=J}$, as theory prescribes above. While the relative influence of the new values for g_{J_N} is increasing for high $J_{N=J}$, the absolute influence is anyways fast approaching zero. For $J_{N=J\pm1}$ energy states, $J \leq 5$ have a large relative difference ($> 1\%$) between old and new calculations. The differences between old and new model are still important up to about $J \leq 10$, as we show later. For higher J, the differences are small between models. Note that $^{16}O_2$ and $^{16}O^{18}O$ will behave the same with the old model, with a small offset as prescribed by their g_S-values in Table 1. The calculations of the new model, however, shows that the isotopologues do behave significantly different at low J. In particular, $^{16}O^{18}O$ has more of a change between old and new models than $^{16}O_2$, with relative offsets of up to 18% for $^{16}O^{18}O$ compared to relative offsets of 16% for $^{16}O_2$.

Of particular interest to the atmospheric research community is the potential errors that might have been introduced into for-

ward computations by the simplified g_{J_N}-coefficients. We have prepared Figs. 2 and 3 to briefly address such interests. Note that it is beyond the scope of this work to perform a reanalysis of available measurements. Instead, we have opted to simulate a selection of absorption lines that have been — or are — under active observation by either satellite-borne or ground-based instruments. Fig. 2 shows these absorption lines' cross-section in relative units for the diagonal component of the propagation matrix at combinations of magnetic field strengths of 40 μT and 60 μT, and temperatures of 150 K and 250 K. Fig. 3 shows forward simulations using the American Air Force Geophysics Laboratory (AFGL; [25]) subarctic-winter standard atmospheric conditions at a magnetic field strength of 50 μT for observation geometries similar to what these lines have been — or are — observed at.

Going over the labels in the two figures in detail (see markings in Figs. 2 and 3):

(A) The lower sideband of channel 20 of SSMIS [4,5] have up to 4% differences in cross-sections between new and old g_{J_N}-coefficients (Fig. 2) — closer to the line centers these differences stay below 2%. The 60.43 GHz line is a transition of $^{16}O_2$ from upper state $J'_N = 7_7$ to lower state $J''_N = 8_7$. From Fig. 1 we see that the g-factors of both upper and lower states are significantly improved in the new method. The differences between the models in Fig. 3 are as large as 40 cK in the wings and as low as negative 10 cK closer to the line centers. As SSMIS averages the centers of the lower and upper sideband lines with a width of 1.35 MHz, most of the effect of the new coefficients will be removed.

(B) The upper sideband of channel 20 of SSMIS [4,5] and MAS [6] have up to 1% differences in cross-sections between new and old g_{J_N}-coefficients from Fig. 2 — closer to the line centers these differences reach about 0.5%. The 61.15 GHz line is a transition of $^{16}O_2$ from upper state $J'_N = 9_9$ to lower state $J''_N = 10_9$. Because the higher J_N of this transition compared to the (A) transition, in Fig. 3, as in Fig. 2, the differences are about a quarter for the 61.15 GHz line compared to the 60.43 GHz line using the old or new g_{J_N}. For SSMIS (not shown), this means about 10 cK offsets in the wings and 1 cK offsets closer to the line centers. For MAS (shown), the new g_{J_N}-coefficients affects the forward simulations by about 2 K in Fig. 3. The effects closer to the line centers are small because the signal is saturated. The overall forward simulation effects will thus change at higher limb altitudes.

(C) The 118.75 GHz line is observed in limb view by EOS Aura/MLS [3], and is weakly altered by the new g_{J_N}-coefficients purely due to the inclusion of g_r, having at most 0.05% change in its cross-section in the wings. The 118.75 GHz line is a transition of $^{16}O_2$ from upper state $J'_N = 1_1$ to lower state $J''_N = 0_1$. The latter state is not present in Table 2 because the level 0_1 does not couple to the magnetic field ($g_{0_1} \equiv 0$). The new cross-sections change the brightness temperature in Fig. 3 in a small frequency range by about 20 cK. What this means for the retrieved temperature product by MLS is difficult to say, but it should introduce at most a small bias between temperatures at lower and higher magnetic latitudes.

(D) The 368.5 GHz absorption line, proposed by Larsson et al. [10,11] as a way to observe Martian crustal magnetic fields from an orbiting sub-millimeter sensor, has up to 10% differences in cross-section between old and new g_{J_N}-coefficients. The 368.5 GHz absorption line is a transition from upper state $J'_N = 2_3$ to lower state $J''_N = 1_1$. The 1_1 state is not much changed by the new coefficients as shown by the small effects on the 118.75 GHz absorption line, but the 2_3 state has a change of -4.7% for the new g_{2_3}-coefficient. This results in
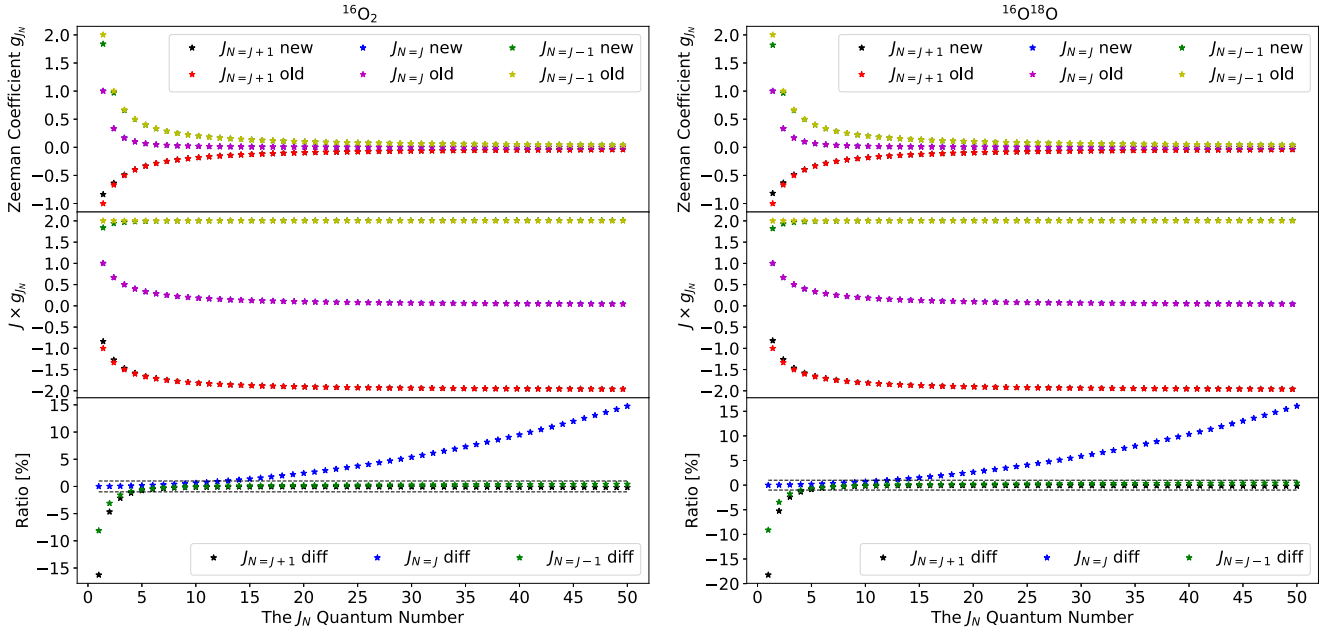
Fig. 1. The change of g_{J_N} with J_N using the new and old theory. First panel shows the absolute value of g_{J_N} for different combinations of $J \in \{N-1, N, N+1\}$ as indicated by the legend, the second panel shows these values multiplied by J to indicate maximum splitting, and the last panel shows the ratio of change between the old and new g_{J_N}-coefficients, with dashed-black lines indicating a 1% limit. The legend should be read such that g_{J_N}-coefficients using Eq. (12) are "new", whereas g_{J_N}-coefficients from Eq. (5) are "old".
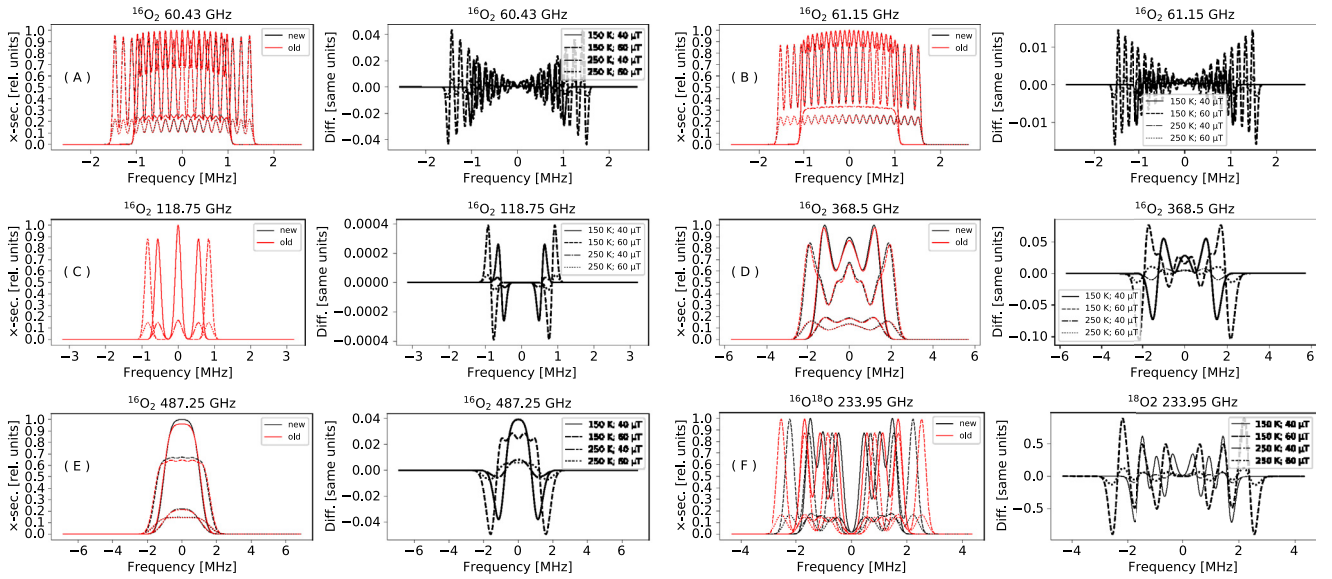

Fig. 2. Difference in unpolarized cross-section for various absorption lines observed by Earth-based instruments. (A) and (B) are averaged as channel 20 of the down-looking SSMIS meteorological instrument. (B) was also measured through the limb by MAS. (C) is observed by the limb-sounding EOS Aura/MLS. (D) was proposed for measuring Mars' crustal magnetism. (E) is observed by the limb-sounding Odin/SMR. Lastly, (F) was observed by ground-based instruments. Each panel contains two plots, the leftmost plot contains normalized cross-sections of the unpolarized component and the rightmost plot shows the difference between using the new coefficients of Table 2 and the old coefficients of Eq. (5). In the left plot, the coefficient origin is indicated by their color as stated in the left legend. The right plots have the same line-style as the leftmost plots, and this line style indicates the considered atmospheric state. The atmospheric pressure is set so low it has minimal effect on the line shape.

a 10 K difference in Fig. 3. While neither Fig. 2 nor 3 is representative of a Mars observational scenario, the improvement in the g_{2_3}-coefficient will prove useful in retrieving accurate magnetic field strengths from measurements of Mars' atmosphere

(E) The 487.25 GHz absorption line observed and resolved by Odin/SMR [2] in limb view has up to 4% differences in cross-section between old and new g_{J_N}-coefficients as seen in

Fig. 2. The 487.25 GHz line is a transition of $^{16}O_2$ from upper state $J'_N = 3_3$ to lower state $J''_N = 2_1$. The 2_1 state is the main cause of the large differences, since g_{2_1} is 3% lower with the new coefficients. In brightness temperatures in Fig. 3, the resulting differences are up to 10 K large. As far as we are aware, no systematic retrieval efforts have been undertaken using this absorption line, so there are no errors to correct.

Table 2

Zeeman coefficients computed for the 50 first J_N energy levels of the two main isotopologue of molecular oxygen. The columns are in order: J_N energy state, g_{J_N} from Eq. (12) for $^{16}O_2$, g_{J_N} from Eq. (12) for $^{16}O^{18}O$, and g_{J_N} from Eq. (5) using g_S for $^{16}O_2$ (these values are 0.003% above Eq. (5) for $^{16}O^{18}O$). This order is repeated thrice each row for $N = J - 1$, $N = J$, and $N = J + 1$, respectively.

J_N	Eq. (12) $^{16}O_2$	Eq. (12) $^{16}O^{18}O$	Eq. (5) g_{J_N}	J_N	Eq. (12) $^{16}O_2$	Eq. (12) $^{16}O^{18}O$	Eq. (5) g_{J_N}	J_N	Eq. (12) $^{16}O_2$	Eq. (12) $^{16}O^{18}O$	Eq. (5) g_{J_N}
1_0	1.839435	1.819754	2.002084	1_1	1.0011	1.001076	1.001042	1_2	−0.838219	−0.818553	−1.001042
2_1	0.970122	0.96625	1.001042	2_2	0.333777	0.333776	0.333681	2_3	−0.636229	−0.632349	−0.667361
3_2	0.656846	0.655471	0.667361	3_3	0.166947	0.166951	0.16684	3_4	−0.489783	−0.488394	−0.500521
4_3	0.495924	0.495287	0.500521	4_4	0.100214	0.100221	0.100104	4_5	−0.395594	−0.39494	−0.400417
5_4	0.398126	0.397782	0.400417	5_5	0.066848	0.066856	0.066736	5_6	−0.331162	−0.3308	−0.333681
6_5	0.33246	0.332254	0.333681	6_6	0.047782	0.04779	0.047669	6_7	−0.284562	−0.284338	−0.286012
7_6	0.285348	0.285217	0.286012	7_7	0.035865	0.035874	0.035751	7_8	−0.249366	−0.249216	−0.25026
8_7	0.24991	0.249823	0.25026	8_8	0.027921	0.02793	0.027807	8_9	−0.221873	−0.221767	−0.222454
9_8	0.222292	0.222232	0.222454	9_9	0.02236	0.022369	0.022245	9_{10}	−0.199816	−0.199736	−0.200208
10_9	0.200164	0.200122	0.200208	10_{10}	0.018316	0.018325	0.018201	10_{11}	−0.181733	−0.181671	−0.182008
11_{10}	0.18204	0.18201	0.182008	11_{11}	0.015282	0.015292	0.015167	11_{12}	−0.166642	−0.166592	−0.16684
12_{11}	0.166924	0.166902	0.16684	12_{12}	0.012949	0.012959	0.012834	12_{13}	−0.153859	−0.153818	−0.154006
13_{12}	0.154125	0.154109	0.154006	13_{13}	0.011116	0.011125	0.011	13_{14}	−0.142893	−0.142858	−0.143006
14_{13}	0.143148	0.143137	0.143006	14_{14}	0.009649	0.009659	0.009534	14_{15}	−0.133383	−0.133352	−0.133472
15_{14}	0.133631	0.133624	0.133472	15_{15}	0.008458	0.008467	0.008342	15_{16}	−0.125058	−0.125031	−0.12513
16_{15}	0.125301	0.125296	0.12513	16_{16}	0.007476	0.007486	0.007361	16_{17}	−0.117708	−0.117684	−0.11777
17_{16}	0.117948	0.117946	0.11777	17_{17}	0.006658	0.006668	0.006543	17_{18}	−0.111174	−0.111152	−0.111227
18_{17}	0.111411	0.11141	0.111227	18_{18}	0.00597	0.00598	0.005854	18_{19}	−0.105325	−0.105305	−0.105373
19_{18}	0.10556	0.105561	0.105373	19_{19}	0.005384	0.005394	0.005269	19_{20}	−0.10006	−0.100041	−0.100104
20_{19}	0.100294	0.100296	0.100104	20_{20}	0.004883	0.004892	0.004767	20_{21}	−0.095295	−0.095278	−0.095337
21_{20}	0.095528	0.095531	0.095337	21_{21}	0.004449	0.004459	0.004334	21_{22}	−0.090963	−0.090946	−0.091004
22_{21}	0.091196	0.091199	0.091004	22_{22}	0.004072	0.004082	0.003957	22_{23}	−0.087007	−0.086991	−0.087047
23_{22}	0.087239	0.087243	0.087047	23_{23}	0.003743	0.003753	0.003627	23_{24}	−0.08338	−0.083365	−0.08342
24_{23}	0.083612	0.083617	0.08342	24_{24}	0.003453	0.003462	0.003337	24_{25}	−0.080043	−0.080028	−0.080083
25_{24}	0.080274	0.08028	0.080083	25_{25}	0.003196	0.003206	0.00308	25_{26}	−0.076962	−0.076948	−0.077003
26_{25}	0.077194	0.077199	0.077003	26_{26}	0.002968	0.002978	0.002852	26_{27}	−0.07411	−0.074096	−0.074151
27_{26}	0.074341	0.074347	0.074151	27_{27}	0.002764	0.002774	0.002648	27_{28}	−0.07146	−0.071447	−0.071503
28_{27}	0.071691	0.071698	0.071503	28_{28}	0.002582	0.002591	0.002466	28_{29}	−0.068994	−0.06898	−0.069037
29_{28}	0.069224	0.069231	0.069037	29_{29}	0.002417	0.002427	0.002301	29_{30}	−0.066691	−0.066678	−0.066736
30_{29}	0.066922	0.066929	0.066736	30_{30}	0.002269	0.002279	0.002153	30_{31}	−0.064537	−0.064525	−0.064583
31_{30}	0.064768	0.064775	0.064583	31_{31}	0.002134	0.002144	0.002018	31_{32}	−0.062518	−0.062505	−0.062565
32_{31}	0.062749	0.062756	0.062565	32_{32}	0.002012	0.002022	0.001896	32_{33}	−0.060621	−0.060608	−0.060669
33_{32}	0.060852	0.060859	0.060669	33_{33}	0.0019	0.00191	0.001784	33_{34}	−0.058835	−0.058823	−0.058885
34_{33}	0.059066	0.059074	0.058885	34_{34}	0.001798	0.001808	0.001682	34_{35}	−0.057152	−0.05714	−0.057202
35_{34}	0.057382	0.05739	0.057202	35_{35}	0.001705	0.001715	0.001589	35_{36}	−0.055561	−0.055549	−0.055613
36_{35}	0.055792	0.0558	0.055613	36_{36}	0.001619	0.001629	0.001503	36_{37}	−0.054057	−0.054045	−0.05411
37_{36}	0.054288	0.054296	0.05411	37_{37}	0.00154	0.00155	0.001424	37_{38}	−0.052632	−0.05262	−0.052686
38_{37}	0.052863	0.052871	0.052686	38_{38}	0.001467	0.001477	0.001351	38_{39}	−0.05128	−0.051268	−0.051335
39_{38}	0.051511	0.051519	0.051335	39_{39}	0.001399	0.001409	0.001283	39_{40}	−0.049995	−0.049984	−0.050052
40_{39}	0.050226	0.050235	0.050052	40_{40}	0.001337	0.001347	0.001221	40_{41}	−0.048774	−0.048762	−0.048831
41_{40}	0.049004	0.049013	0.048831	41_{41}	0.001279	0.001288	0.001163	41_{42}	−0.04761	−0.047598	−0.047669
42_{41}	0.047841	0.047849	0.047669	42_{42}	0.001224	0.001234	0.001109	42_{43}	−0.0465	−0.046489	−0.04656
43_{42}	0.046731	0.04674	0.04656	43_{43}	0.001174	0.001184	0.001058	43_{44}	−0.045441	−0.04543	−0.045502
44_{43}	0.045672	0.045681	0.045502	44_{44}	0.001127	0.001137	0.001011	44_{45}	−0.044429	−0.044418	−0.044491
45_{44}	0.04466	0.044669	0.044491	45_{45}	0.001083	0.001093	0.000967	45_{46}	−0.043461	−0.04345	−0.043524
46_{45}	0.043692	0.043701	0.043524	46_{46}	0.001042	0.001052	0.000926	46_{47}	−0.042534	−0.042523	−0.042598
47_{46}	0.042765	0.042774	0.042598	47_{47}	0.001003	0.001013	0.000887	47_{48}	−0.041645	−0.041634	−0.04171
48_{47}	0.041876	0.041885	0.04171	48_{48}	0.000967	0.000977	0.000851	48_{49}	−0.040793	−0.040782	−0.040859
49_{48}	0.041024	0.041033	0.040859	49_{49}	0.000933	0.000943	0.000817	49_{50}	−0.039975	−0.039964	−0.040042
50_{49}	0.040206	0.040215	0.040042	50_{50}	0.000901	0.000911	0.000785	50_{51}	−0.039189	−0.039178	−0.039257

(F) The 233.95 GHz line observed by Pardo et al. [8] using ground-based radiometry has a difference in cross-section for old and new g_{J_N}-coefficients of up to 60%. The 233.95 GHz line is a transition of $^{16}O^{18}O$ from upper state $J'_N = 1_2$ to lower state $J''_N = 1_0$. The low J_N, as well as both state being $J_{N=J\pm1}$-states, is by Fig. 1 why the differences are so large as they are between the new and old line shapes. The 1_2 state has a difference in its g_{1_2}-coefficient of about 18.2%, and the 1_0 state has a difference in its g_{1_0}-coefficient of about 9.1%. Using Eq. (14), these differences means that using the new g_{J_N}-coefficients is computationally equivalent to reducing the magnetic field strength by $18.2 - 9.1 = 9.1\%$. In Fig. 3, the brightness temperature differences are only 20 cK, but it is clear what impact the 9.1% reduction in frequency shift has on the overall line shape.

In fact, we want to draw special attention to that [8] inversed their measurements to retrieve the magnetic field strength above their radiometer. Their results were a retrieved magnetic field strength of 44 μT, but a model of the magnetic field strength at the time predicted the magnetic field strength to be 40 μT. Since this $40/44 - 1 = -9.1\%$ is the same as the differences in g_{J_N}-coefficients, we induce that the retrievals [8] performed were adequate for the task of retrieving the magnetic field strength but that their input model Zeeman data were incorrect. Had they used the g_{J_N}-coefficients that we present in this work, by our reasoning from Eq. (14), they would have retrieved a magnetic field strength of 40 μT. At that point, any offset from the model magnetic field might be deduced to be from external sources not available in the instantaneous magnetic field
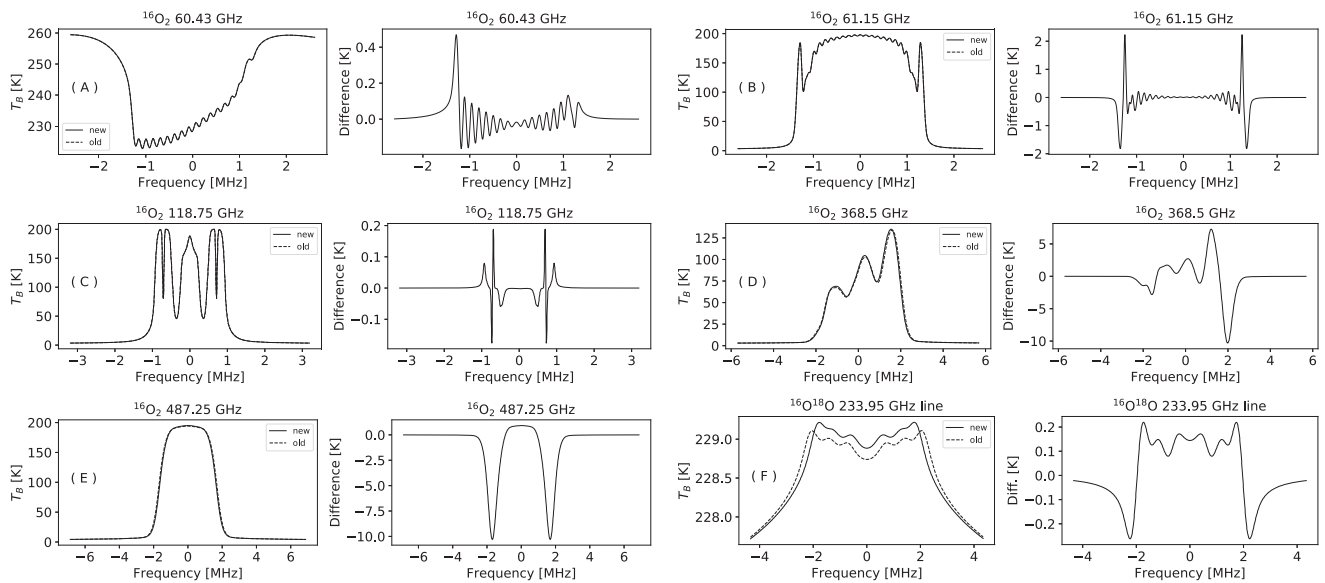
Fig. 3. Difference in brightness temperatures for a subarctic-winter AFGL atmospheric scenario at 50 μT for the absorption lines found in Fig. 2, with the same labels except that we only show limb geometry results for (B). The left panel shows forward simulations using both the new and old splitting coefficients and the right panel shows model differences. Panels (B,C) and (E,F) show linear polarization and panels (A) and (D) shows circular polarization. Panel (A) shows a satellite line-of-sight at 135° off-zenith, panels (B-E) shows limb observations with a tangent altitude of 85 km, and panel (F) shows a ground-based observation geometry at an elevation angle of 15°.

model, such as inductive currents in the ionosphere by aurora, or recoupling in the magnetic tail. This last statement obviously needs more measurements, inversions, and comparisons with other instrumentations to confirm, as other sources of error might present themselves.

5. Conclusions

We present updated Zeeman effect splitting coefficients using detailed calculations for molecular oxygen. We show simulations of cross-section and brightness temperature effects on molecular oxygen using the more detailed Zeeman splitting coefficient computations, comparing them to the so far common atmospheric community approach of applying simplified Zeeman splitting coefficient for said computations. Our simulation results show that there are potential problems for absorption lines with low $J_{N\neq J}$-numbers using the simplified pure Hund case (b) approach. This is seen clearly for the 368.5 GHz, 487.75 GHz, and 233.95 GHz absorption lines having the largest change in our case study. Lines with intermediately large $J_{N\neq J}$-numbers — in the case study the 60.43 GHz and 61.15 GHz absorption lines — have a much smaller change in their profiles, though still significant if frequency resolved. Absorption lines with large $J_{N\neq J}$-numbers are barely affected by this simplification. Energy states with $J_{N=J}$ have a small systematic difference between the detailed and simplified approach resulting in very small offsets in brightness temperatures, as shown by the 118.75 GHz case study absorption line.

We have not shown any direct validation in this work that the detailed computations of the splitting coefficients are better than the simplified approach, although the theoretical improvement they represent strongly speaks for their superiority. Aside from theoretical arguments, we conclude from induction that the detailed computations offer better representation of the molecular oxygen Zeeman effect. Our logic follows from Eq. (14), that if Pardo et al. [8] had used the detailed coefficients then they would have retrieved a magnetic field strength 9.1% weaker than they did. Instead, they used the simplified coefficients and retrieved a magnetic field strength that was 9.1% greater than the predictions of an

independent model. Based on both the theoretical improvements they represent, and the apparent improvement for retrieving magnetic field strength, we recommend that future efforts that measures molecular oxygen in the mesosphere at terahertz and lower frequencies make use of the coefficients we publish here in their forward modeling and subsequent retrieval efforts.

References

[1] Zeeman P. On the influence of magnetism on the nature of the light emitted by a substance. Astrophys J 1897;5:332–47.

[2] Murtagh D, Frisk U, Merino F, Ridal M, Jonsson A, Stegman J, et al. An overview of the Odin atmospheric mission. Can J Phys 2002;80(4):309–19. doi:10.1139/P01-157.

[3] Schwartz MJ, Read WG, Snyder WV. EOS MLS forward model polarized radiative transfer for Zeeman-split oxygen lines. IEEE Trans Geosci Remote Sens 2006;44(3):1182–91.

[4] Kunkee DB, Poe GA, Boucher DJ, Swadley SD, Hong Y, Wessel JE, et al. Design and evaluation of the first special sensor microwave imager/sounder. IEEE Geosci Remote Sens 2008;46(4):863–83.

[5] Swadley SD, Poe GA, Bell W, Hong Y, Kunkee DB, McDermid IS, et al. Analysis and characterization of the SSMIS upper atmosphere sounding channel measurements. IEEE Geoscience and Remote Sensing 2008;46(4):962–83.

[6] Hartmann GK, Degenhardt W, Richards ML, Liebe HJ, Hufford GA, Cotton MG, et al. Zeeman splitting of the 61 gigahertz oxygen (O$_2$) line in the mesosphere. Geophys Res Lett 1996;23(17):2329–32.

[7] Navas-Guzmán F, Kämpfer N, Murk A, Larsson R, Buehler SA, Eriksson P. Zeeman effect in atmospheric O$_2$ measured by ground-based microwave radiometry. Atmos Meas Tech 2015;8(4):1863–74. doi:10.5194/amt-8-1863-2015.

[8] Pardo J, Pagani L, Gerin M, Prigent C. Evidence of the Zeeman splitting in the $21 \rightarrow 01$ rotational transition of the atmospheric 16O18O molecule from ground-based measurements. J Quant Spectrosc Radiat Transfer 1995;54(6):931–43. doi:10.1016/0022-4073(95)00129-9.

[9] Yee JH, Gjerloev J, Wu D, Schwartz MJ. First application of the Zeeman technique to remotely measure auroral electrojet intensity from space. Geophys Res Lett 2017;44(20):10,134–10,139. doi:10.1002/2017GL074909.

[10] Larsson R, Ramstad R, Mendrok J, Buehler SA, Kasai Y. A method for remote sensing of weak planetary magnetic fields: Simulated application to Mars. Geophys Res Lett 2013;40(19):5014–18. doi:10.1002/grl.50964.

[11] Larsson R, Milz M, Eriksson P, Mendrok J, Kasai Y, Buehler SA, et al. Martian magnetism with orbiting sub-millimeter sensor: simulated retrieval system. Geosci Instrum Methods Data Syst 2017;6(1):27–37. doi:10.5194/gi-6-27-2017.

[12] Lenoir WB. Propagation of partially polarized waves in a slightly anisotropic medium. J Appl Phys 1967;38(13):5283–90.

[13] Lenoir WB. Microwave spectrum of molecular oxygen in the mesosphere. J Geophys Res 1968;73(1):361–76.

[14] Liebe HJ. Modeling attenuation and phase of radio waves in air at frequencies below 1000 GHz. Radio Sci 1981;16(06):1183–99. doi:10.1029/RS016i006p01183.

[15] Rosenkranz PW, Staelin DH. Polarized thermal microwave emission from oxygen in the mesosphere. Radio Sci 1988;23(5):721–9. doi:10.1029/RS023i005p00721.

[16] Larsson R, Buehler SA, Eriksson P, Mendrok J. A treatment of the Zeeman effect using Stokes formalism and its implementation in the Atmospheric Radiative Transfer Simulator (ARTS). J Quant Spectrosc Radiat Transfer 2014;133:445–53. doi:10.1016/j.jqsrt.2013.09.006.

[17] Drouin BJ, Yu S, Miller CE, Müller HS, Lewen F, Brünken S, et al. Terahertz spectroscopy of oxygen, O_2, in its $^3\Sigma_g^-$ and $^1\Delta$ electronic states: THz spectroscopy of O_2. J Quant Spectrosc Radiat Transfer 2010;111(9):1167–73. Special Issue Dedicated to Laurence S. Rothman on the Occasion of his 70th Birthday. 10.1016/j.jqsrt.2009.12.006

[18] Bowers KD, Kamper RA, Lustig CD. Paramagnetic resonance absorption in molecular oxygen. Proc R Soc Lond A: Math Phys Eng Sci 1959;251(1267):565–74. doi:10.1098/rspa.1959.0129.

[19] Christensen H, Veseth L. On the high-precision Zeeman effect in O_2 and SO. J Mol Spectrosc 1978;72(3):438–44. doi:10.1016/0022-2852(78)90142-X.

[20] Brown JM, Carrington A. Rotational spectroscopy of diatomic molecules. Cambridge University Press; 2003. doi:10.1017/CBO9780511814808.

[21] Johansson H, Forssén C. Fast and accurate evaluation of Wigner 3j, 6j, and 9j symbols using prime factorization and multiword integer arithmetic. SIAM J Scientif Comput 2016;38(1):A376–84. doi:10.1137/15M1021908.

[22] Larsson R. A note on modelling of the oxygen spectral cross-section in the Atmospheric Radiative Transfer Simulator Zeeman effect combined with line mixing in the earths atmosphere. Int J Remote Sens 2014;35(15):5845–53. doi:10.1080/01431161.2014.945002.

[23] Eriksson P, Buehler S, Davis C, Emde C, Lemke O. ARTS, the atmospheric radiative transfer simulator, version 2. J Quant Spectrosc Radiat Transfer 2011;112(10):1551–8. doi:10.1016/j.jqsrt.2011.03.001.

[24] Buehler SA, Mendrok J, Eriksson P, Perrin A, Larsson R, Lemke O. ARTS, the Atmospheric Radiative Transfer Simulator – version 2.2, the planetary toolbox edition. Geosci Model Dev 2018;11(4):1537–56. doi:10.5194/gmd-11-1537-2018.

[25] Anderson GP, Clough SA, Kneizys FX, Chetwynd JH, Shettle EP. AFGL atmospheric constituent profiles (0–120 km). Tech. Rep. AFGL; 1986. TR-86-0110